Optimized Natural-Laminar-Flow Airfoils

J. Driver* and D. W. Zingg†
University of Toronto Institute for Aerospace Studies
4925 Dufferin Street, Toronto, Ontario
Canada, M3H 5T6

A two-dimensional Newton-Krylov aerodynamic shape optimization algorithm has been modified to incorporate the prediction of laminar-turbulent transition. Modifications to the discrete-adjoint gradient computation were required to allow the optimization algorithm to manipulate the transition point through shape changes. The coupled Euler and boundary-layer solver, MSES, is used to obtain transition locations, which are then used in Optima2D, a Newton-Krylov discrete-adjoint optimization algorithm based on the compressible Reynolds-averaged Navier-Stokes equations. The algorithm is applied to the design of airfoils with maximum lift-drag ratio, endurance factor, and lift coefficient. The design examples demonstrate that the optimizer is able to control the transition point locations to provide optimum performance, in effect designing optimized natural-laminar-flow airfoils. In particular, the optimization algorithm is able to design an airfoil that is very similar, in terms of both shape and performance, to one of the high-lift airfoils designed by Liebeck (*J. of Aircraft*, 10:610-617, 1973) in the 1970's.

I. Introduction

Numerical optimization techniques based on either gradient-based adjoint methods or genetic algorithms have proven to be a powerful tool in aerodynamic design.[1–4] Most existing optimization algorithms which are based on the Reynolds-averaged Navier-Stokes equations assume that the flow is fully turbulent, i.e. laminar-turbulent transition is assumed to occur at the leading edge.[2,3,5–7] Therefore, the optimizer cannot exploit the effect of the airfoil shape on the location of transition in maximizing the objective function. Consequently, these algorithms cannot optimize natural-laminar-flow airfoils, where significant regions of laminar flow are achieved through a suitable pressure gradient.

Prior to the development of efficient and robust aerodynamic optimization techniques, high-performance airfoils could be designed by determining a pressure distribution that is feasible and optimal in some sense and using an inverse method to find the corresponding airfoil shape. For example, the Stratford concave pressure distribution, which leads to incipient turbulent boundary-layer separation, can be used to produce the shortest region of pressure recovery possible without separation. Liebeck[8] used both laminar and turbulent rooftops followed by Stratford-type pressure recovery to design several high-lift airfoils. Zingg[9] designed an airfoil for high lift-to-drag ratio by combining a rooftop with a pressure gradient chosen to maintain laminar flow with a concave pressure recovery determined by requiring a constant boundary-layer shape factor. The constant shape factor permits a margin from separation to be chosen, leading to rapid pressure recovery without incipient separation. The airfoils designed in these two studies achieve very high performance. Their design is a complex process involving considerable knowledge of aerodynamics. This suggests the following question: Can such airfoils be designed automatically using an aerodynamic optimization technique? There are two aspects to the question. The first issue is whether the optimizer is able to find such a unique and specialized optimum. The second is whether the airfoils designed by Liebeck and Zingg are actually optimal in some sense, i.e. can the optimizer do better?

The objectives of the current work are as follows:

*Aeronautical Engineer, Pratt & Whitney Canada, AIAA Member, jonathan.driver@pwc.ca
†Professor, Senior Member AIAA, Tier I Canada Research Chair in Computational Aerodynamics, http://goldfinger.utias.utoronto.ca/dwz

- To incorporate laminar-turbulent transition prediction into Optima2D, the Newton-Krylov discrete-adjoint aerodynamic optimization algorithm of Nemec and Zingg,[2,3] which is based on the Reynolds-averaged Navier-Stokes (RANS) equations, and to investigate airfoils designed to minimize various objective functions.
- To investigate whether the numerical optimization algorithm can design airfoils comparable to those designed by Liebeck and Zingg.

Our focus is on the optimized airfoils and their performance. At this stage, we are not as concerned with the efficiency of the algorithm. An efficient discrete-adjoint algorithm incorporating transition prediction requires a prediction methodology that can be effectively integrated into a RANS solver, such as that of Langtry and Menter.[10] Furthermore, the airfoils presented here have been optimized for performance at a single operating point and consequently are not suitable for practical use, which requires consideration of off-design performance as well. Related research combining transition prediction with aerodynamic optimization has been presented by Drela,[11] Dodbele,[12] Green at al.,[13] Pralits,[14] and Sturdza.[15,16]

II. Methodology

The extension of the Spalart-Allmaras (SA) turbulence model to include the laminar-turbulent trip functions is fairly straightforward and is discussed in the Newton-Krylov framework by Chisholm and Zingg.[18] An overview of the required modifications to the SA turbulence model and how the transition locations are obtained is explained in the next section. The method through which the transition locations affect the gradient is explained in the section entitled Gradient Evaluation.

A. Newton-Krylov Flow Solver

The two-dimensional compressible Navier-Stokes equations in conjunction with a one-equation turbulence model are solved using a Newton-Krylov approach with approximate factorization start-up. The development of the complete SA model in the approximately-factored and Newton-Krylov frameworks is discussed in Godin et al.,[19] and Zingg et al.,[20] respectively. The required modifications to the SA model are briefly discussed below. The complete SA turbulence model in steady-state form, rewritten for clarity, takes the following form:

$$J^{-1}\left[M(\tilde{\nu}) - P(\tilde{\nu}) + D(\tilde{\nu}) - N(\tilde{\nu})\right] = 0 \tag{1}$$

where $M(\tilde{\nu})$, $P(\tilde{\nu})$, $D(\tilde{\nu})$, and $N(\tilde{\nu})$ are the convection, production, destruction and diffusion terms, respectively. Only the production and destruction terms are modified to include trip terms:

$$P(\tilde{\nu}) = \frac{c_{b1}}{\mathcal{R}e}\tilde{S}\tilde{\nu}\left(1 - f_{t2}\right) + \mathcal{R}e f_{t1}\Delta U^2 \tag{2}$$

$$D(\tilde{\nu}) = \left(\frac{c_{w1}f_w}{\mathcal{R}e} - \frac{c_{b1}f_{t2}}{\kappa^2\mathcal{R}e}\right)\left(\frac{\tilde{\nu}}{d_{\mathrm{w}}}\right)^2 \tag{3}$$

The factor of J^{-1} is introduced to improve the scaling of the flow Jacobian matrix. It is important to note that the Spalart-Allmaras turbulence model does not predict the transition location. Furthermore, the addition of the trip term, $\mathcal{R}e f_{t1}\Delta U^2$, in Eq. 2 acts as a source for the evolution of turbulent growth in the boundary layer. The discretization of equation Eq. 1 was unmodified from the fully turbulent version. Details can be found in Nemec.[17] It should be noted that the trip function (f_{t_1}) is not included in the flow Jacobian and only exists in the residual equations. Chisholm and Zingg showed that the added differentiation of this trip function affects convergence only slightly.[21]

In order to obtain accurate transition locations, a complete solution from MSES[11] is obtained. A value of 9 is used as the critical amplification factor value (N). The transition locations are then used in the RANS flow solve. This is done in order to avoid the difficulty of fully coupling an e^N method into the RANS solution. In order for this approach to be effective, the pressure distributions of the MSES and RANS solutions should be similar.

B. Gradient Evaluation

We solve the aerodynamic shape optimization problem using a gradient-based approach. The details of the algorithm can be found in Nemec and Zingg.[2] We modify the discrete-adjoint gradient calculation in the following manner:

$$\frac{d\mathcal{J}}{d\mathcal{X}} = \frac{\partial \mathcal{J}}{\partial \mathcal{X}} - \psi^T \frac{\partial \mathcal{R}}{\partial \mathcal{X}} + \frac{\partial \mathcal{J}}{\partial \mathcal{T}} \frac{\partial \mathcal{T}}{\partial \mathcal{X}} \tag{4}$$

where $\mathcal{J}$ is the objective function, $\mathcal{X}$ are the design variables, T are the transition point locations, and ψ is the adjoint variable. The sensitivity of the objective function with respect to the transition location movement, $\frac{\partial \mathcal{J}}{\partial \mathcal{T}}$, is combined, via the chain rule, with the movement of the transition location due to airfoil perturbations, $\frac{\partial \mathcal{T}}{\partial \mathcal{X}}$. This product contains the contribution of the upper and lower transition location sensitivities, which are denoted by the subscripts "up" and "lo":

$$\frac{\partial \mathcal{J}}{\partial \mathcal{T}} \frac{\partial \mathcal{T}}{\partial \mathcal{X}} = \frac{\partial \mathcal{J}}{\partial T_{lo}} \frac{\partial T_{lo}}{\partial \mathcal{X}} + \frac{\partial \mathcal{J}}{\partial T_{up}} \frac{\partial T_{up}}{\partial \mathcal{X}} \tag{5}$$

A first-order backward finite-difference approximation of the $\frac{\partial \mathcal{J}}{\partial \mathcal{T}}$ term is used for both the upper and lower airfoil surfaces:

$$\frac{\partial \mathcal{J}}{\partial T_{lo}} = \frac{\mathcal{J}\left[X, Q\right] - \mathcal{J}\left[X, Q(X, T_{lo} - h)\right]}{h} \tag{6}$$

$$\frac{\partial \mathcal{J}}{\partial T_{up}} = \frac{\mathcal{J}\left[X, Q\right] - \mathcal{J}\left[X, Q(X, T_{up} - h)\right]}{h} \tag{7}$$

$\frac{\partial T_{up}}{\partial \mathcal{X}}$ and $\frac{\partial T_{lo}}{\partial \mathcal{X}}$ are found via finite differences of airfoil perturbations using MSES. It is important to note that equations 6 and 7 require a new RANS flow solve for each perturbed state, while $\frac{\partial T}{\partial \mathcal{X}}$ requires one MSES flow solve per design variable perturbation. Since we are using MSES to calculate the $\frac{\partial \mathcal{T}}{\partial \mathcal{X}}$ term, it is important to eliminate as much introduced error in the calculation of this term as possible. This is done by reducing the viscous residual in MSES to 10^{-6}. From numerical experiments, the transition locations have converged beyond eight significant digits. Further details regarding the algorithm can be found in Driver.[22]

III. Results and Discussion

A. Objective Functions

The following objective functions are considered. In each case, geometric constraints are added to the objective function as penalty terms.

1. maximization of the lift-to-drag ratio:

$$\mathcal{J} = \frac{C_L}{C_D} \tag{8}$$

2. endurance factor maximization:

$$\mathcal{J} = \frac{C_L^{3/2}}{C_D} \tag{9}$$

3. maximization of lift coefficient, C_L, with and without some additional penalty terms in the objective function.

B. Lift to Drag Ratio Maximization

The NACA 0012 airfoil is used as the initial airfoil for the maximization of the lift-to-drag ratio. A single-block, structured C-grid is used with roughly 18,500 nodes, 220 on the airfoil surface. The off-wall spacing is

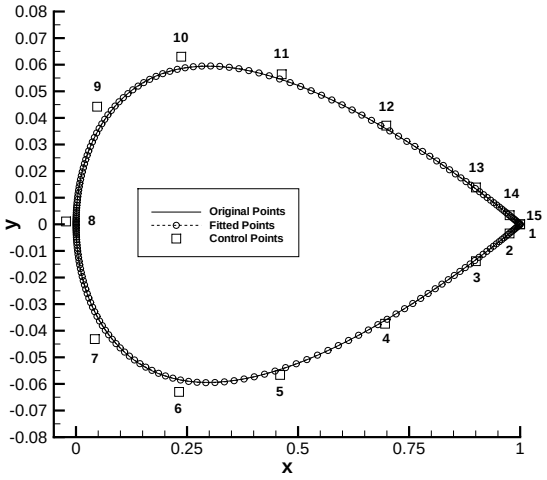

Figure 1. NACA 0012: control points and design variables

Table 1. Lift-to-Drag Maximization: Cases 1 and 2

Case	$\frac{C_L}{C_D}$	T_{up} (x/c)	T_{lo} (x/c)	Airfoil Area	Angle of Attack
Case $1_{initial}$	31.38	0.45	0.85	0.08073	2.00^o
Case 1_{final}	101.22	0.57	0.95	0.08081	4.23^o
Case $2_{initial}$	28.85	0.18	0.49	0.08073	2.00^o
Case 2_{final}	101.60	0.29	0.95	0.08075	5.86^o

1×10^{-6}, the distance to the outer boundary is 24, and the spacing at the stagnation point and trailing edge is 1×10^{-4}, where all distances are expressed in terms of the airfoil chord length. The airfoil is parameterized using 15 B-spline control points, of which 12 are used as design variables; the locations are indicated in Figure 1. Control points 2-7 are used as design variables on the lower surface, with control points 9-14 used as design variables on the upper surface. The angle of attack is also included as a design variable. The area of the initial airfoil is required to be preserved throughout the optimization process. The area constraint is lifted into the objective function via a penalty method with a weight of 0.1.

Two cases are optimized using the above initial conditions, but with different operating conditions. **Case 1** is optimized at a Mach number of 0.25 and a Reynolds number of 1 million, while **Case 2** is optimized at a Mach number of 0.4 and a Reynolds number of 10 million. In both cases the initial angle of attack is set to 2 degrees. Table 1 lists the lift-to-drag ratios, transition locations, and area values for both the initial and final airfoils. Note that the transition points are constrained to lie no further aft than 95% chord.

Figures 2 and 3 show the initial and final airfoils and pressure distributions. **Case 1** shares similar qualities found in high lift-to-drag ratio airfoils at similar operating conditions.[9] The entire lower surface experiences laminar flow, while transition occurs at approximately 57% chord on the upper surface. **Case 2** shows how the Reynolds number affects the optimum, since transition is very sensitive to the Reynolds number. Similar to **Case 1**, the entire lower surface experiences laminar flow. In order to push the transition location further downstream the favourable pressure gradient on the upper surface is required to be steeper than in the lower Reynolds number case. This favorable pressure gradient adds stability to the boundary layer, allowing transition to occur further aft.

A lift-to-drag ratio maximization for Reynolds numbers ranging from 1 to 10 million at a Mach number of 0.25 is presented in Figure 4. Table 2 lists the associated lift-to-drag ratio values, transition locations, and angles of attack for all of the cases. This experiment was done to examine how the pressure distribution on the upper surface reacts to provide boundary layer stability at different Reynolds numbers. As the

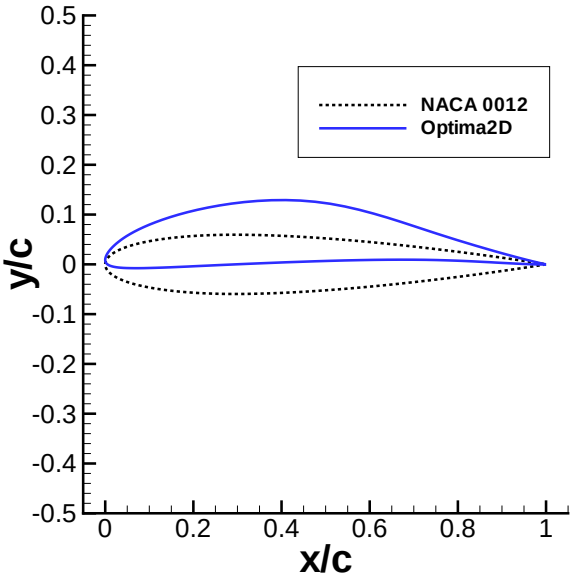

(a) Initial and final airfoils

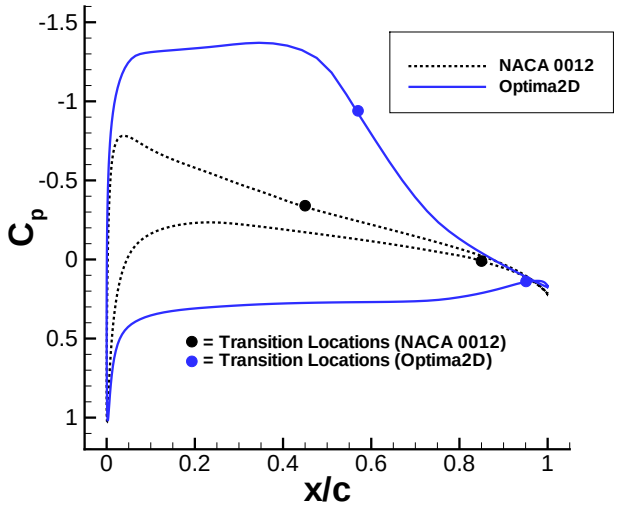

(b) Initial and final pressure distributions

Figure 2. Case 1: Lift-to-drag ratio maximization, M=0.25, Re=1 million

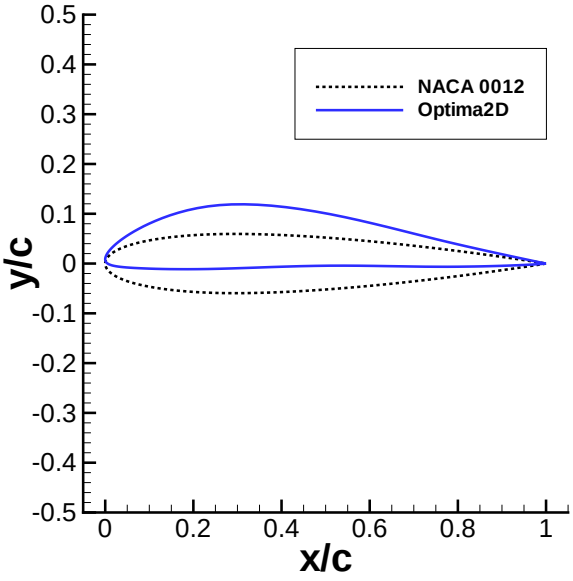

(a) Initial and final airfoils

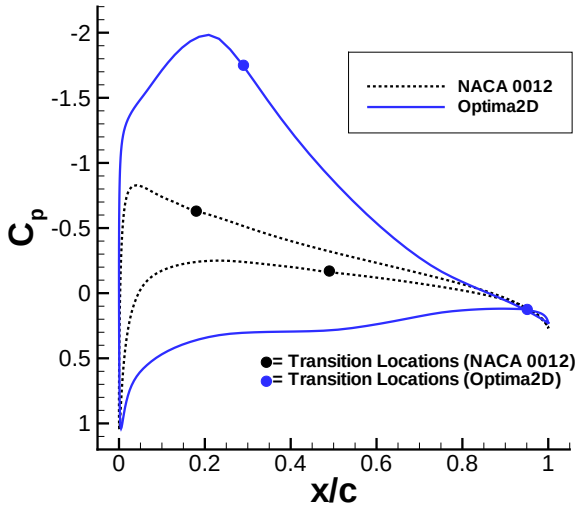

(b) Initial and final pressure distributions

Figure 3. Case 2: Lift-to-drag ratio maximization, M=0.40, Re=10 million

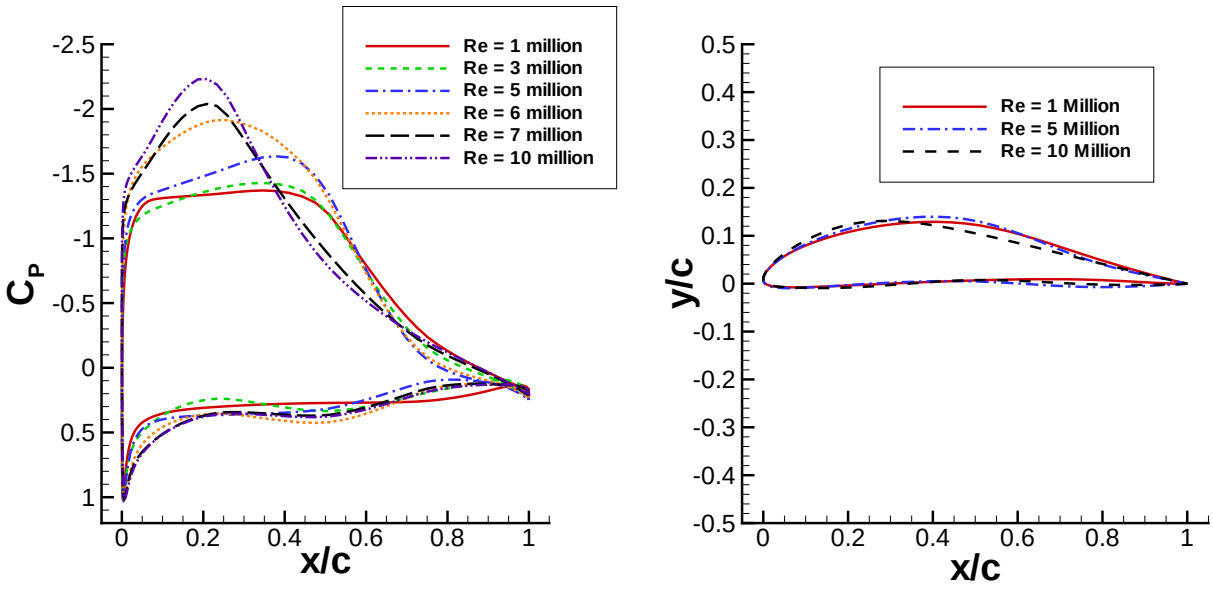

(a) Pressure distributions

(b) Sample airfoils

Figure 4. Lift-to-drag ratio maximization: Reynolds number variations

Table 2. Lift-to-drag ratio maximization: Reynolds number variation

Reynolds Number (10^6)	$\frac{C_L}{C_D}$	T_{up} (x/c)	T_{lo} (x/c)	Angle of Attack
1.0	101.22	0.57	0.95	4.23^o
3.0	118.40	0.53	0.95	4.64^o
5.0	117.32	0.51	0.95	5.35^o
6.0	112.02	0.43	0.95	6.34^o
7.0	102.27	0.31	0.95	6.33^o
10.0	100.20	0.29	0.95	6.80^o

Reynolds number increases, the favourable pressure gradient on the upper surface gradually becomes steeper to maintain boundary-layer stability, as expected.

C. Endurance Factor Maximization

The general-aviation airfoil, GA(W)-1, is used as the initial airfoil for the endurance factor maximization. A single-block, structured C-grid is used with roughly 14,000 nodes, 201 on the airfoil surface. The remaining grid details are identical to the lift-to-drag ratio maximization case above. The airfoil is parameterized using 15 B-spline control points, of which 6 are used as design variables. The angle of attack is also included as a design variable. Table 3 shows the thickness constraints used to avoid invalid shapes during the optimization iterations. The thickness constraints are lifted into the objective function via a penalty method with a weight of 1.0.

Two cases are optimized using the above initial conditions, but under different operating conditions. **Case 3** is optimized under fully turbulent conditions at a Mach number of 0.2 and a Reynolds of 2 million. **Case 4** is optimized at the same Mach and Reynolds numbers with free transition. **Case 3** is the 7 design-variable case presented by Hua et al.[23] In both cases, the initial angle of attack is set to 2 degrees. Table 4

Table 3. Endurance factor maximization: thickness constraints

x/c	0.15	0.35	0.60	0.92	0.99
t/c	0.01	0.164	0.07	0.01	0.001

Table 4. Endurance factor maximization: Cases 3 and 4

Case	$\frac{C_L^{3/2}}{C_D}$	T_{up} (x/c)	T_{lo} (x/c)	Angle of Attack
Case $3_{initial}$	49.24	-	-	7.53^o
Case 3_{final}	59.83	-	-	7.24^o
Case $4_{initial}$	61.99	0.49	0.65	2.44^o
Case 4_{final}	115.50	0.54	0.92	5.97^o

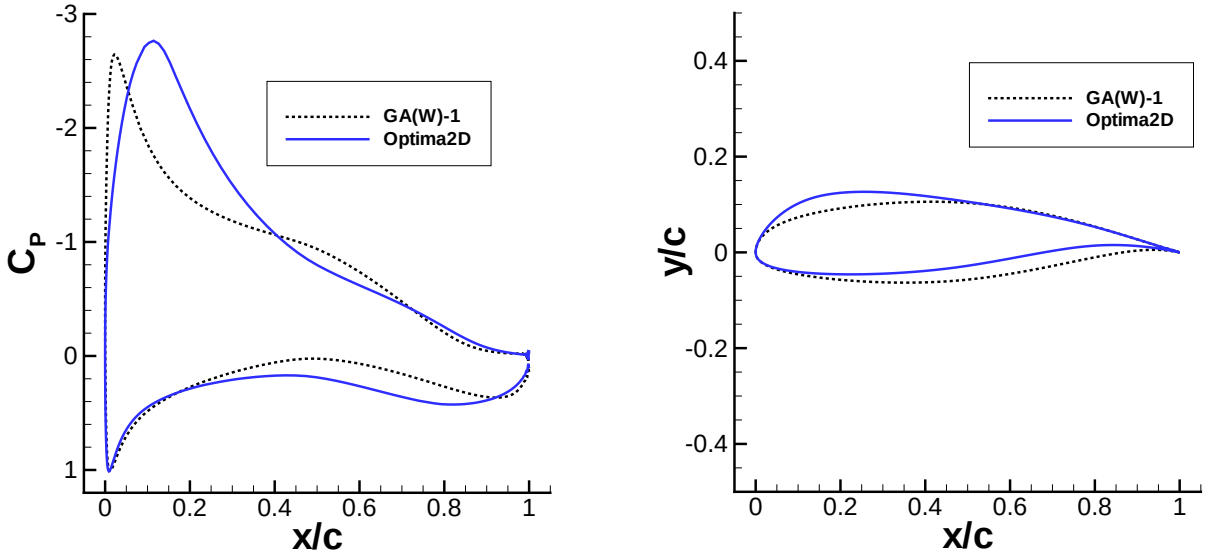

(a) Initial and final pressure distributions

(b) Initial and final airfoils

Figure 5. Case 3: Endurance factor maximization, fully turbulent, M=0.2, Re=2 million

lists the endurance factor, lift, drag, transition locations, and angle of attack for both the initial and final airfoils. The initial and final airfoils and pressure distributions for **Case 3** are shown in Fig. 5; results for **Case 4** are presented in Fig. 6. In both cases, the initial angle-of-attack is chosen to maximize the endurance factor for the GA(W)-1 airfoil under the specified conditions, i.e. fully-turbulent or with free transition.

In both design cases the thickness constraint at 35% chord is the only active constraint at convergence. By exploiting a substantial region of laminar flow on both surfaces, **Case 4** is able to produce an airfoil that has an endurance factor nearly double that of the fully turbulent case. Although this demonstrates a far superior airfoil at these operating conditions, off-design conditions can have a detrimental impact on the performance. For example, when the airfoil designed in **Case 4** is analyzed under fully turbulent conditions, the steep pressure recovery causes turbulent boundary-layer separation, and the drag pays an enormous penalty. Obviously this is not a desirable aerodynamic property. It is desirable to design an airfoil

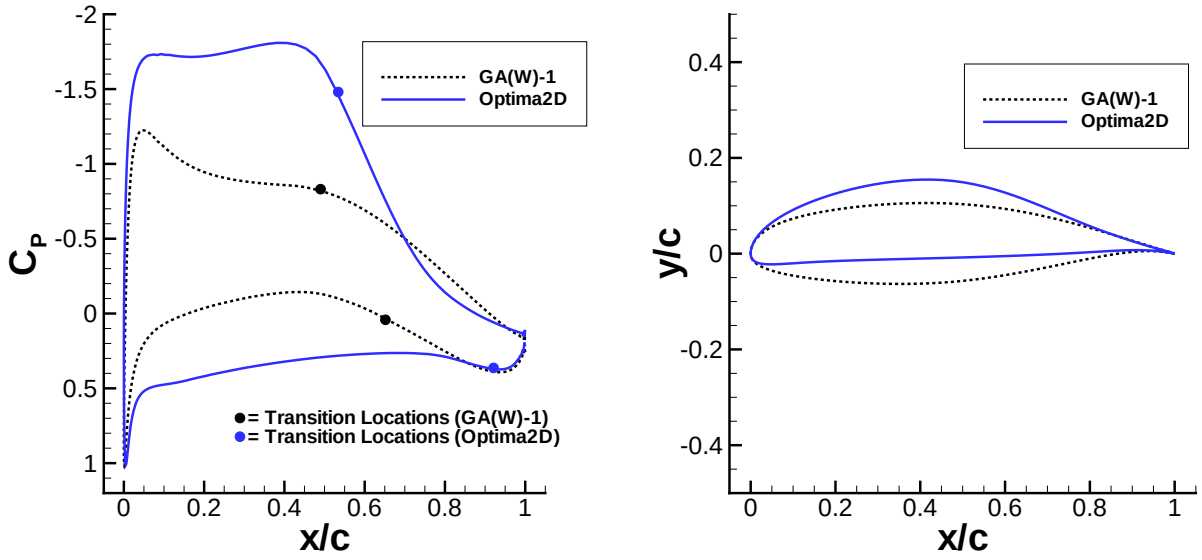

(a) Initial and final pressure distributions

(b) Initial and final airfoils

Figure 6. Case 4: Endurance factor maximization, free transition, M=0.2, Re=2 million

that exploits the advantages of having maximum laminar flow under ideal conditions but also performs well when transition occurs further forward than expected. These trade-offs can be assembled into a family of non-inferior designs, or a Pareto front.

In order to form a Pareto front, the weighted-sum method is used:

$$\mathcal{J} = \omega_{ft}\mathcal{J}_{ft} + (1-\omega_{ft})\,\mathcal{J}_{lt} + \omega_t \sum_{j=1}^{N_c} C_j \tag{10}$$

where $\mathcal{J}_{ft}$ and $\mathcal{J}_{lt}$ are the objective function values of Eq. 9 under fully turbulent and laminar-turbulent conditions, respectively, the C_j are geometric constraints, and $\omega_t = 1.0$. An important point to make is that at each Pareto front location a two-point design problem is solved. The two points are a laminar-turbulent analysis and a fully turbulent analysis. The initial conditions are identical to **Cases 3** and **4**. The computed Pareto front is shown in Figure 7, where the trade-offs associated with favoring one operating condition over the other are clearly captured. Figure 8 shows selected Pareto front airfoils and the laminar-turbulent pressure distributions. Table 5 lists the coefficients of lift and drag for the selected solutions contained in the Pareto front.

Interesting trade-offs between fully turbulent and laminar-turbulent designs can be understood through this Pareto front. For example, if one is aggressive and uses ω_{ft}=0.1, then one pays a huge price if transition occurs at the leading edge; the endurance factor drops from approximately 115 to 49. If one is conservative and uses ω_{ft}=0.9, then the gain when laminar flow is achieved is minimal. With intermediate values of ω_{ft}, for example $0.3 \leq w_{ft} \leq 0.7$, the off-design performance improves without too large a penalty in on-design performance. For example, with ω_{ft}=0.5, the fully turbulent endurance factor is approximately 56 while the on-design laminar-turbulent endurance factor is approximately 107.

D. Maximization of Lift Coefficient

In this section, three different lift-maximization problems are considered. In each case, the NACA 0012 airfoil is the initial airfoil. A single-block, structured C-grid is used with roughly 25,000 nodes, 325 on the airfoil surface. The remaining grid details and geometry parameterization are identical to the lift-to-drag

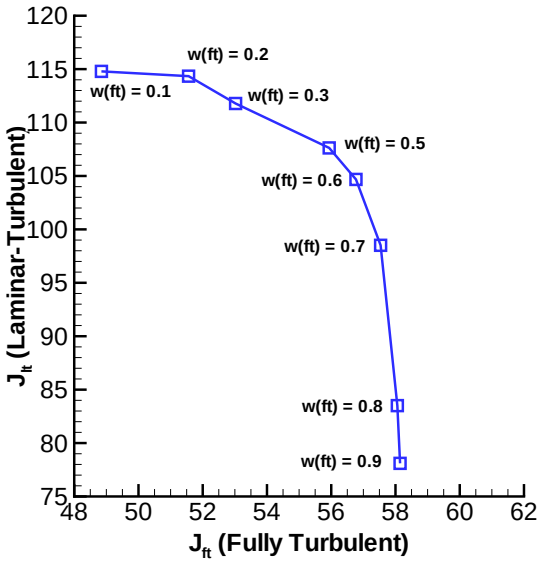

Figure 7. Pareto front: laminar-turbulent versus fully turbulent endurance factor maximization

Table 5. Aerodynamic coefficients and endurance factor values for selected Pareto optimal solutions

ω_{ft}	Fully-Turbulent C_L	Fully-Turbulent C_D	Laminar-Turbulent C_L	Laminar-Turbulent C_D	Fully-Turbulent $\frac{C_L^{3/2}}{C_D}$	Laminar-Turbulent $\frac{C_L^{3/2}}{C_D}$
0.1	1.088	0.0233	1.384	0.0142	48.84	114.7
0.2	1.127	0.0232	1.383	0.0142	51.55	114.2
0.3	1.126	0.0225	1.285	0.0130	53.02	111.7
0.5	1.213	0.0239	1.292	0.0137	55.90	107.5
0.6	1.259	0.0249	1.212	0.0128	56.72	104.4
0.7	1.235	0.0239	1.105	0.0118	57.48	98.34
0.8	1.270	0.0247	1.134	0.0145	57.96	83.31
0.9	1.308	0.0257	1.036	0.0135	58.01	77.86

ratio maximization cases. Table 6 shows the thickness constraints used. The thickness constraints are lifted into the objective function via a penalty method with a weight of 0.05.

For the first lift-maximization example, designated **Case 5**, the following objective function is used:[24]

$$\mathcal{J} = \omega_L \left(1 - \frac{C_L}{C_L^*}\right)^2 + \omega_t \sum_{j=1}^{N_c} C_j \tag{11}$$

where C_L^* is a target lift coefficient chosen as 2.10. The results of this optimization are given in Table 7 and Fig. 9. A lift coefficient of 2.09 is achieved with turbulent boundary-layer separation at 86% chord on the upper surface. The pressure distribution on the upper surface has a sort of laminar rooftop followed by concave pressure recovery. There is a favourable pressure gradient over the entire lower surface.

For the second lift-maximization example, designated **Case 6**, a constraint on the skin-friction coefficient

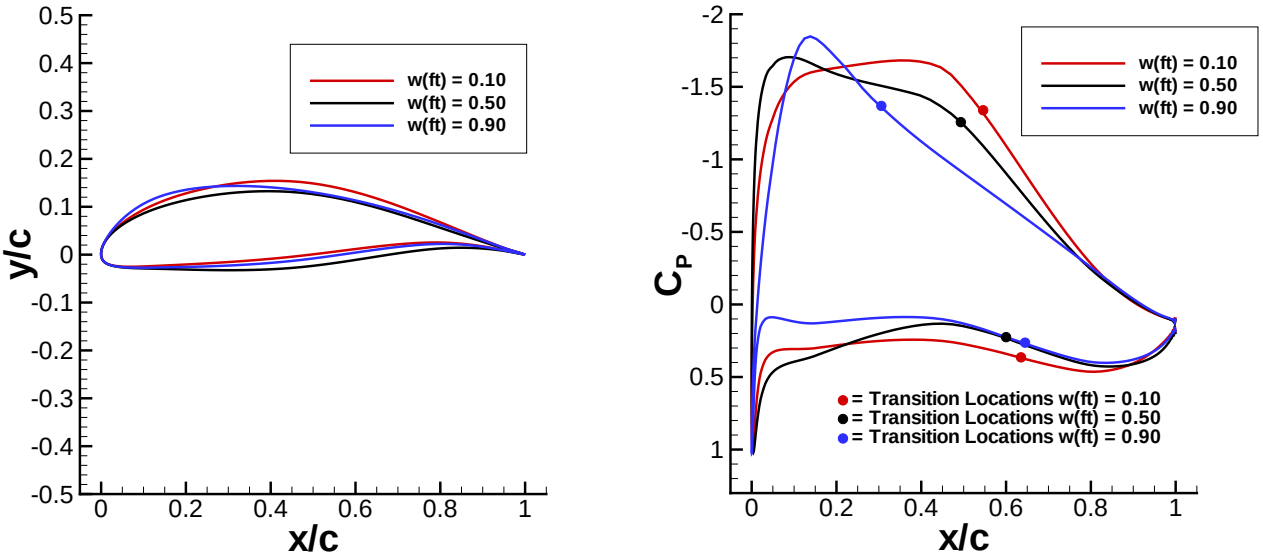

(a) Selected Pareto front airfoils

(b) Selected Pareto front laminar-turbulent pressure distributions

Figure 8. Selected Pareto optimal solutions

Table 6. Maximization of lift: thickness constraints

x/c	0.06	0.25	0.60	0.80	0.95
t/c	0.08	0.10	0.055	0.02	0.01

Table 7. Maximization of lift: Case 5

Case	C_L	C_D	T_{up} (x/c)	T_{lo} (x/c)	Angle of Attack
Case $5_{initial}$	0.2188	0.0066	0.37	0.75	2.00^o
Case 5_{final}	2.0937	0.0277	0.36	0.95	11.70^o

is added in the following manner:

$$\mathcal{J} = \omega_L \left(1 - \frac{C_L}{C_L^*}\right)^2 + \sum_{x=x_{start}}^{x_{end}} \left(\omega_{cf} \left(1 - \frac{c_{cf}(x)}{c_f^*(x)}\right)^2\right) + \omega_t \sum_{j=1}^{N_c} C_j \tag{12}$$

where c_f^* is a target skin-friction coefficient over a specified range of the airfoil surface from x_{start} to x_{end}. Note that the skin-friction constraint is active only when violated, i.e. when the local skin friction dips below the specified value. The following parameters are used: $C_L^* = 1.72$, $c_f^* = 0.001$, $\omega_L = 2.0$, $\omega_{cf} = 1.0$. This constraint ensures that the flow remains fully attached. Results are given in Table 8 and Fig. 10. With the requirement of fully attached flow, the maximum lift coefficient achieved is 1.69. The upper surface pressure distribution displays a significant favourable gradient in the laminar region followed by concave pressure recovery. The lower surface again has a favourable pressure gradient throughout.

For our third lift-maximization example, **Case 7**, the pitching moment is constrained, and the require-

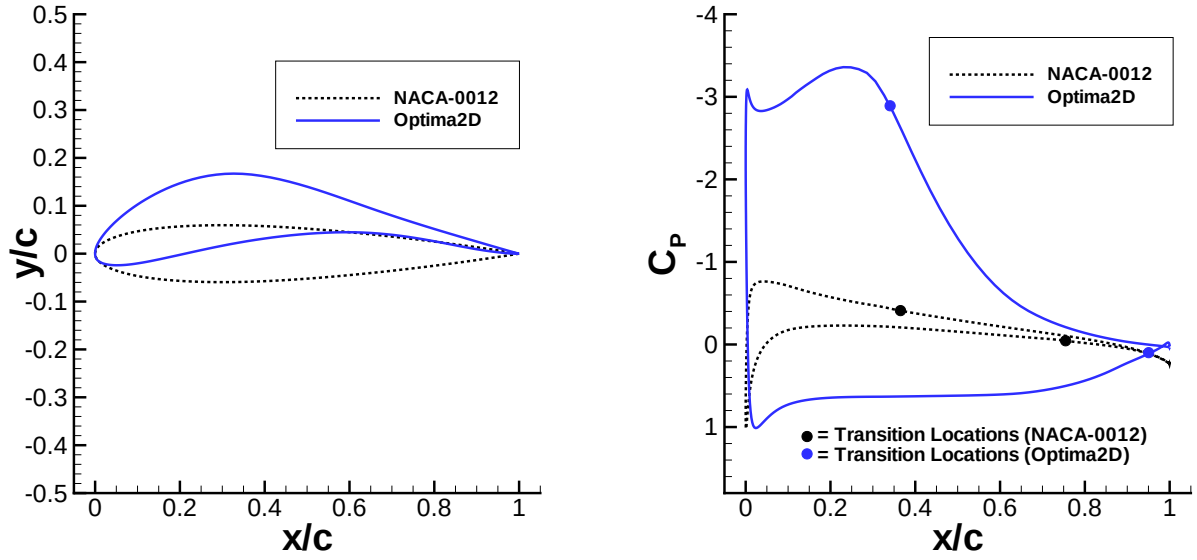

(a) Initial and final airfoils

(b) Initial and final pressure distributions

Figure 9. Case 5: Maximization of lift, M=0.25, Re=2 Million

Table 8. Maximization of lift with separation constraint: Case 6

Case	C_L	C_D	T_{up} (x/c)	T_{lo} (x/c)	Angle of Attack
Case $6_{initial}$	0.2188	0.0066	0.37	0.75	2.00^o
Case 6_{final}	1.6937	0.0181	0.38	0.95	8.56^o

ment of attached flow is retained, leading to the following objective function:

$$\mathcal{J} = \omega_L \left(1 - \frac{C_L}{C_L^*}\right)^2 + \omega_M \left(1 - \frac{C_M}{C_M^*}\right)^2 + \sum_{x=x_{start}}^{x_{end}} \left(\omega_{cf} \left(1 - \frac{c_f(x)}{c_f^*(x)}\right)^2\right) + \omega_t \sum_{j=1}^{N_c} C_j \tag{13}$$

The moment constraint is nonzero only if the pitching moment coefficient exceeds the target value, C_M^* (in magnitude). The following parameters are used: $C_L^* = 1.60$, $C_M^* = -0.032$, $c_f^* = 0.001$, $\omega_L = 2.0$, $\omega_M = 1.0$, $\omega_{cf} = 1.0$. The optimized airfoil and associated pressure distribution are shown in Fig. 11; further data are given in Table 9. The reduction in the magnitude of the moment coefficient has led to a reduction of the lift coefficient to 1.58. The upper surface pressure distribution has a laminar rooftop with a pressure coefficient of roughly -2.50 followed by concave pressure recovery. The lower surface has a more pronounced favourable pressure gradient than the two previous cases, leading to decreased aft loading and consequently a reduced pitching moment. The lower surface of the airfoil is flat, in contrast to the concave lower surfaces of the optimized airfoils of **Cases 5 and 6**.

Fig. 12 compares the lift, drag, and moment coefficients of the optimized airfoils of **Cases 5, 6, and 7** as a function of angle of attack. In comparison with **Case 5**, the additional skin friction coefficient constraint in **Case 6** has caused a reduction in maximum lift coefficient, a reduction in drag coefficient, and a reduction in the magnitude of the pitching moment coefficient. The addition of the pitching moment constraint in **Case 7** has resulted in the same trends. Therefore, of the three optimized airfoils, **Case 7** has the lowest maximum lift coefficient, the lowest drag coefficient, and the smallest pitching moment coefficient.

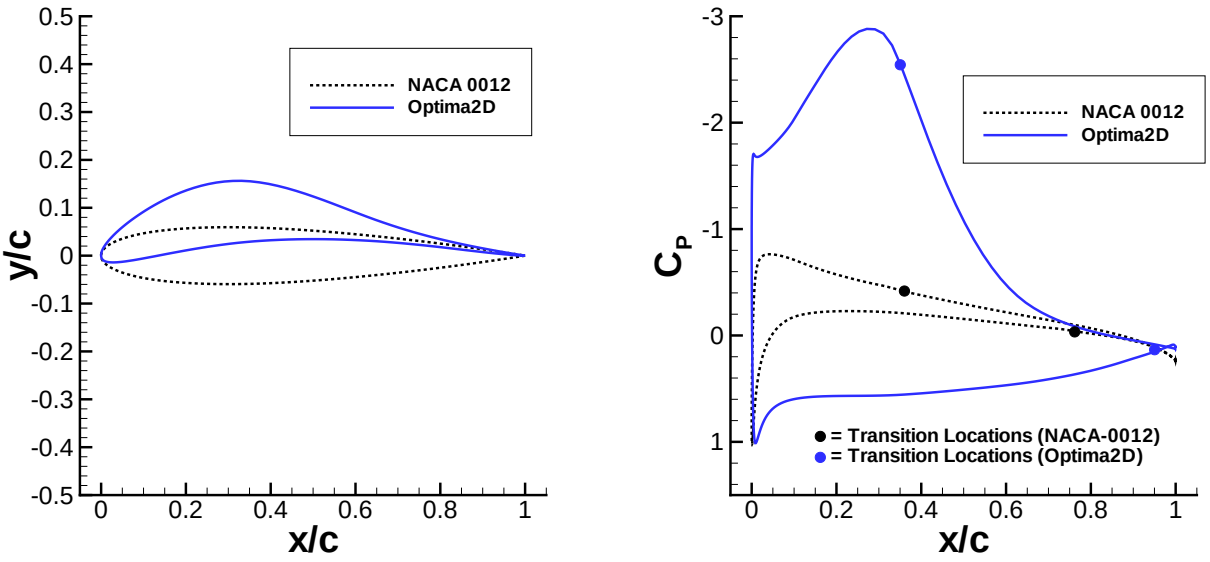

(a) Initial and final airfoils

(b) Initial and final pressure distributions

Figure 10. Case 6: Maximization of lift with separation constraint, M=0.25, Re=2 Million

Table 9. Maximization of lift with pitching moment and separation constraints: Case 7

Case	C_L	C_M	T_{up} (x/c)	T_{lo} (x/c)	Angle of Attack
Case $7_{initial}$	0.2188	0.0028	0.37	0.75	2.00^o
Case 7_{final}	1.5812	-0.0324	0.33	0.95	10.06^o

E. Comparison with Zingg and Liebeck Airfoils

The previous examples have demonstrated that the optimization algorithm is capable of exploiting the location of transition to optimize the airfoil. The resulting pressure distributions correspond closely to what might be expected: some sort of laminar rooftop followed by a concave pressure recovery region. In this section, we compare two optimized airfoils with airfoils designed using a carefully determined pressure distribution and an inverse method, those of Liebeck[8] and Zingg.[9]

The Liebeck airfoil, LNV109A, was designed to maximize the lift coefficient with fully attached flow and a practical and realistic shape. The objective function and constraints for **Case 7** have been chosen to mimic those of Liebeck. The two airfoils as well as the pressure distributions at the optimum angle of attack are compared in Fig. 13. With the exception of a small region near the leading edge, both the airfoils and the pressure distributions are strikingly similar. The lift, drag, and moment coefficients produced by the two airfoils are nearly identical, as shown in Fig. 12.

In order to compare with the Zingg airfoil, we mimic the thickness constraint used in its design by requiring that the maximum thickness be 15% of the chord without specifying the chordwise position. Fig. 14 displays the resulting airfoils and pressure distributions. They are again very similar, although the Zingg airfoil has a somewhat steeper pressure recovery and transition further aft on the upper surface. The Zingg airfoil has a lift-to-drag ratio of 83 at $C_L = 0.888$, which occurs at an angle of attack of 1.93°. The optimized airfoil has a lift-to-drag ratio of 90 and $C_L = 0.9974$ at an angle of attack of 4.28°. The optimized airfoil has a larger lift-to-drag ratio, but Fig. 14 shows that it has a slightly smaller cross-sectional area.

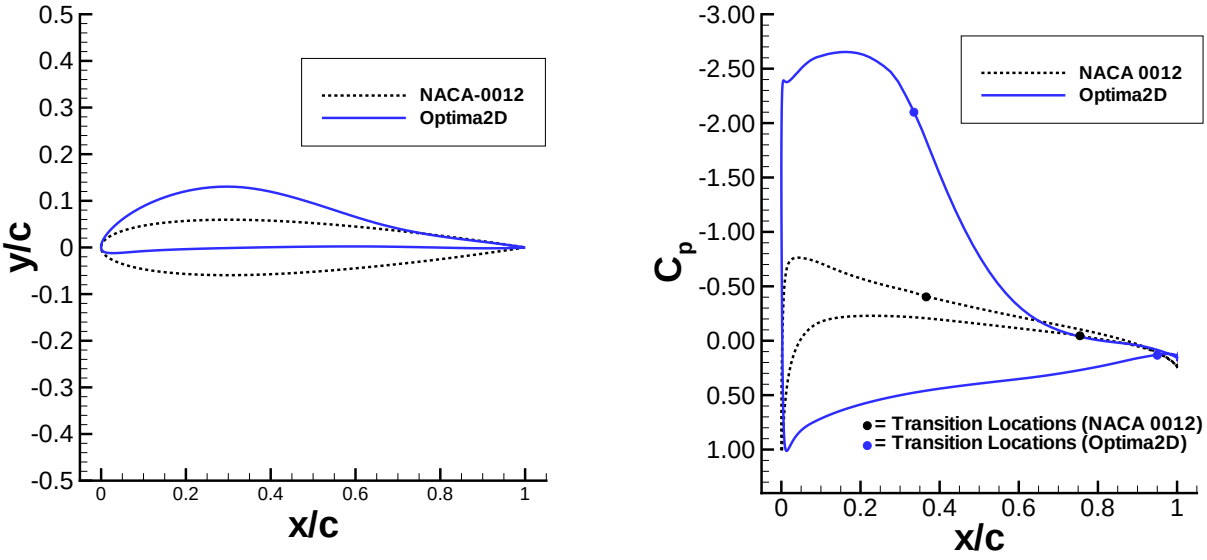

(a) Initial and final airfoils

(b) Initial and final pressure distributions

Figure 11. Case 7: Maximization of lift with pitching moment and separation constraints, M=0.25, Re=2 Million

IV. Conclusions

We have presented aerodynamic optimization results which incorporate laminar-turbulent transition. These results show that the optimizer is able to exploit the transition location to obtain improvements in the objective function. The resulting optimized natural-laminar-flow airfoils have characteristics very similar to airfoils designed previously based on considerable aerodynamic expertise, such as those of Liebeck and Zingg. Future work will involve integrating the transition prediction module with the RANS solver to enable full exploitation of the discrete-adjoint method.

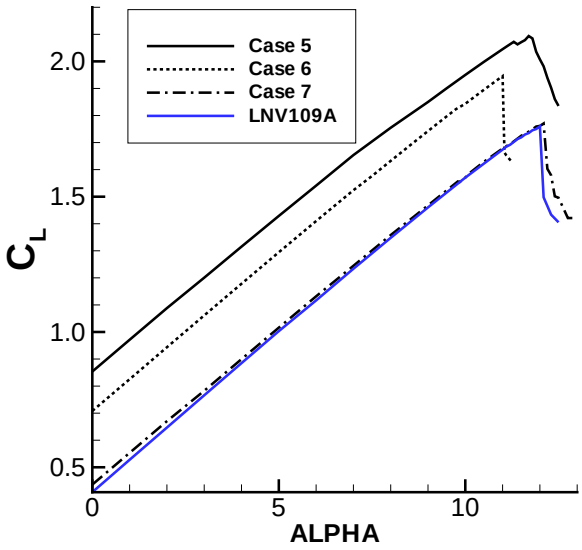

(a) C_L variation

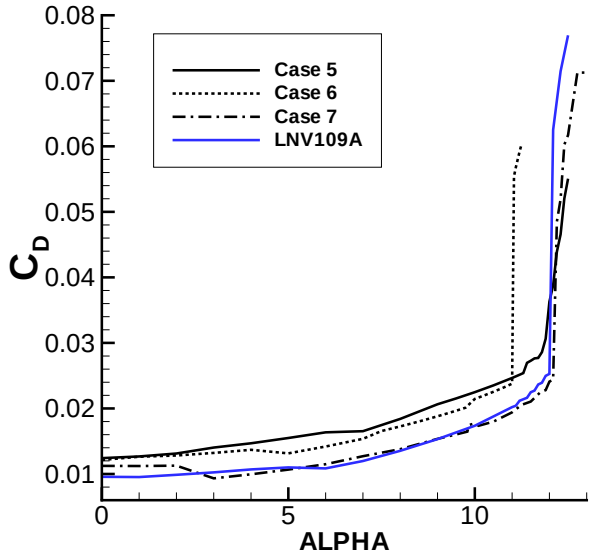

(b) C_D variation

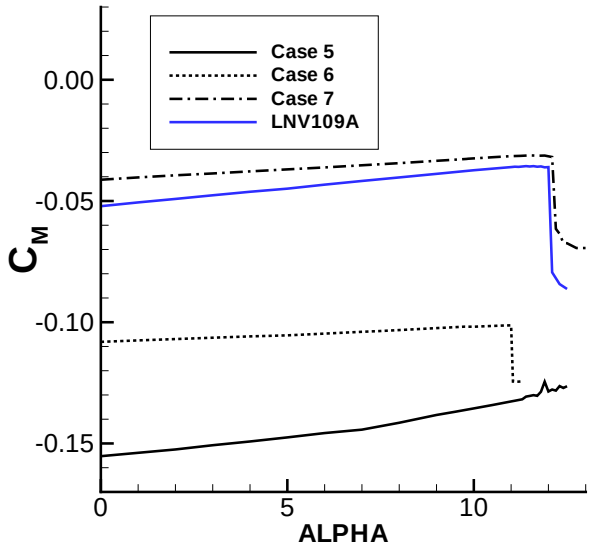

(c) C_M variation

Figure 12. Comparison of lift-maximization cases and Liebeck airfoil (LNV109A), M=0.25, Re=2 Million

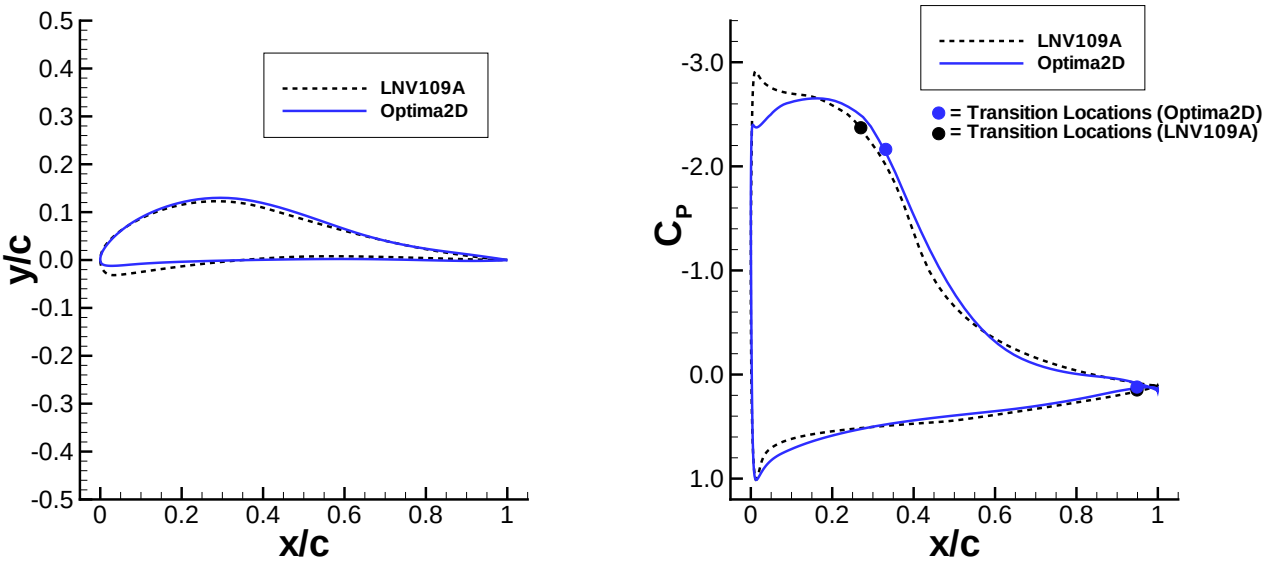

(a) Airfoils (b) Pressure distributions

Figure 13. Comparison of Liebeck airfoil LNV109A with Case 7, M=0.25, Re=2 Million

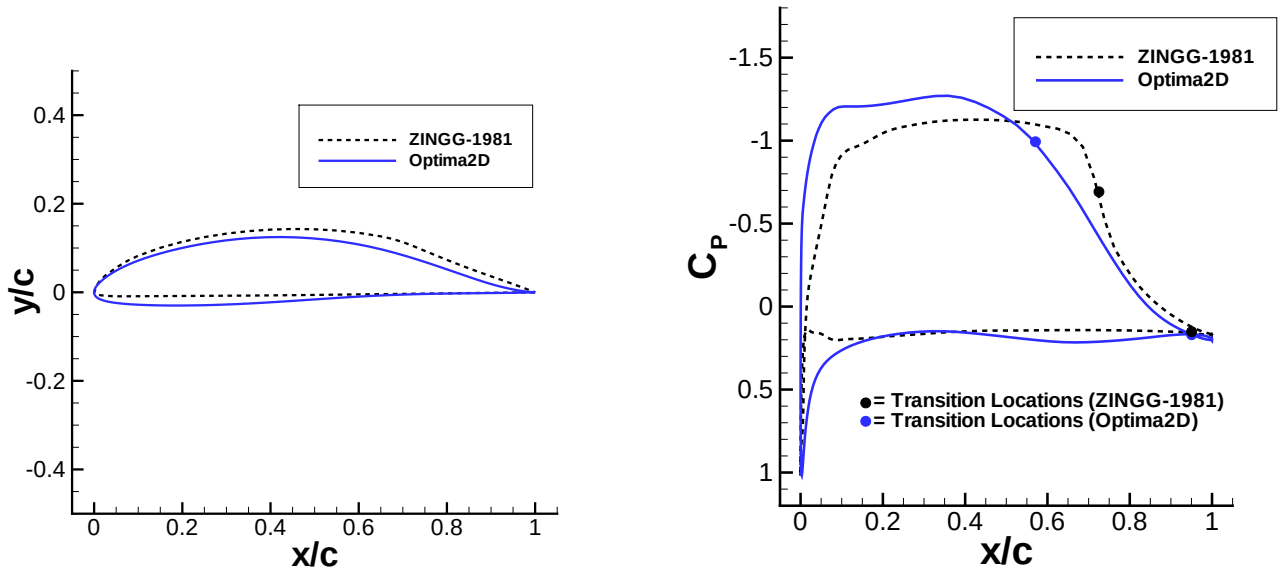

(a) Airfoils (b) Pressure distributions

Figure 14. Comparison of Zingg airfoil with optimized airfoil, M=0.25, Re=1 Million

References

[1]Jameson, A., "Aerodynamic Design via Control Theory," NASA CR-181749, No. 1988.

[2]Nemec, M. and Zingg, D. W., "Newton–Krylov Algorithm for Aerodynamic Design Using the Navier–Stokes Equations," *AIAA Journal*, Vol. 40, No. 6, 2002, pp. 1146–1154.

[3]Nemec, M., Zingg, D. W., and Pulliam, T.H., "Multipoint and Multi-Objective Aerodynamic Shape Optimization," *AIAA Journal*, Vol. 42, No. 6, 2004, pp. 1057–1065.

[4]Pulliam, T.H., Nemec, M., Holst, T., and Zingg, D.W., "Comparison of Evolutionary (Genetic) Algorithm and Adjoint Methods for Multi-Objective Viscous Airfoil Optimizations," AIAA Paper 2003-0298, Jan. 2003.

[5]Jameson, A., Pierce, N.A., and Martinelli, L., "Optimum Aerodynamic Design Using the Navier-Stokes Equations," *Theoretical and Computational Fluid Dynamics*, Vol. 10, No. 1, 1998, pp. 213-237.

[6]Anderson, W.A., and Bonhaus, D.L., "Airfoil Design on Unstructured Grids for Turbulent Flows," *AIAA J.*, Vol. 37, No. 2, 1999, pp. 185-191.

[7]Elliott, J., and Peraire, J., "Progress Toward a Three-Dimensional Aerodynamic Shape Optimization Tool for the Compressible High Reynolds Number Navier-Stokes Equations Discretized on Unstructured Meshes," AIAA Paper 98-2897, June 1998.

[8]Liebeck, R. H., "A Class of Airfoils Designed for High Lift in Incompressible Flow," *Journal of Aircraft*, Vol. 10, No. 10, 1973, pp. 610–617.

[9]Zingg, D. W., *An Approach to the Design of Airfoils With High Lift to Drag Ratios*, Master's thesis, University of Toronto, 1981.

[10]Langtry, R.B., and Menter, F.R., "Transition Modeling for General CFD Applications," AIAA Paper 2005-0522, Jan. 2005.

[11]Drela, M., "Design and Optimization Method for Multi-Element Airfoils," AIAA Paper 93–0969, 1993.

[12]Dodbele, S. S., "Design Optimization of Natural Laminar Flow Bodies in Compressible Flow," Tech. Rep. 4478, National Aeronautics and Space Administration (NASA), Langley Field, VA., 1993.

[13]Green, B. E., Whitesides, J. L., Campbell, R. L., and Mineck, R. E., "A Method for the Constrained Design of Natural Laminar Flow Airfoils," AIAA Paper 96-2502, 1996.

[14]Pralits, J., *Optimal Design of Natural and Hyrbid Laminar Flow Control on Wings*, Ph.D. thesis, Royal Institute of Technology Department of Mechanics, Stockholm, Sweden, October 2003.

[15]Kroo, I. and Sturdza, P., "Design-Oriented Aerodynamic Analysis for Supersonic Laminar Flow Wings," AIAA Paper 2003-0774, 2003.

[16]Sturdza, P., *An Aerodynamic Design Method for Supersonic Natural Laminar Flow Aircraft*, Ph.D. thesis, Stanford University, 2003.

[17]Nemec, M., *Optimal Shape Design of Aerodynamic Configurations:A Newton-Krylov Approach*, Ph.D. thesis, University of Toronto, 2003.

[18]Chisholm, T. and Zingg, D. W., "A Fully Coupled Newton-Krylov Solver for Turbulent Aerodynamic Flows," Paper 333, ICAS 2002, Toronto, ON, Sept. 2002.

[19]Godin, P., Zingg, D. W., and Nelson, T. E., "High-Lift Aerodynamic Computations with One- and Two-Equation Turbulence Models," *AIAA Journal*, Vol. 35, No. 2, 1997, pp. 237–243.

[20]Zingg, D. W., Nemec, M., and Chisholm, T., "A Newton–Krylov Algorithm for Aerodynamic Analysis and Design," Keynote paper, International Conference on Computational Fluid Dynamics (ICCFD) 2, Sydney, AU, July 2002.

[21]Chisholm, T. and Zingg, D. W., "Start-up Issues in a Newton-Krylov Algorithm for Turbulent Aerodynamic Flows," AIAA Paper 2003-3708, 2003.

[22]Driver, J., "Optimal Aerodynamic Shape Design with Transition Prediction," M.A.Sc. thesis, University of Toronto, 2005.

[23]Hua, J., Liu, P. J., and Zingg, D. W., "Optimization of Long-Endurance Airfoils," AIAA Paper 2003–3500, June 2003.

[24]Nemec, M. and Zingg, D. W., "Optimization of High-Lift Configurations Using a Newton-Krylov Algorithm," AIAA Paper 2003-3957, 2003.